COMPUTATIONAL SIMULATION OF ULTRA-LOW CYCLE FATIGUE FRACTURE OF RING SHAPED – STEEL PLATE SHEAR WALLS

A. Phillips(1), M. Eatherton(2), I. Koutromanos(3),

(1) *Graduate Research Assistant, Virginia Tech, arp12@vt.edu*
(2) *Assistant Professor, Virginia Tech, meather@vt.edu*
(2) *Assistant Professor, Virginia Tech, ikoutrom@vt.edu*

Abstract

Steel structures are a popular solution in earthquake-prone areas, due to their capability for ductile inelastic response under extreme events. The failure and collapse of such structures are typically triggered by steel fracture caused by ultra low-cycle fatigue (ULCF). Analysis methods which can accurately describe the damage accumulation in the material, and the subsequent fracture initiation and propagation are indispensable for the reliable determination of the safety of steel structures. Although a variety of analytical approaches, with varying levels of complexity, have been formulated for describing ULCF in steel components, the finite element method constitutes the most efficient approach.

This paper uses nonlinear finite element models to analytically simulate the response of steel structures. The models are created in commercial finite element programs with constitutive laws which can account for the nonlinear kinematic hardening, the damage accumulation and for the material failure due to ULCF. The fracture propagation is inherently captured in the analytical models, by means of element removal techniques, using a novel, Ring-Shaped Steel Plate Shear Wall (RS-SPSW) concept. RS-SPSWs are a new type of steel plate shear wall that prevent buckling by cutting a pattern of rings connected by diagonal links into a steel plate. The unique ring mechanism delays buckling which leads to improved cyclic energy dissipation and stiffness. The large-scale experiments were 3 meters by 2.6 meters and were subjected to a pseudo-static cyclic loading protocol. The RS-SPSW specimens displayed ductile behavior before developing fractures due to ULCF. Due to the redundant nature of the RS-SPSW system, multiple fractures occurred through the rings before the peak load carrying capacity of the infill panel was significantly reduced. Due to the large number of fractures, these experiments provide a unique opportunity to validate analytical tools as opposed to experiments dominated by one fracture.

Keywords: Ultra-low cycle fatigue, Ring Shaped – Steel Plate Shear Wall, Finite Element Model, Fracture, Damage-plasticity model

1. Introduction

Steel lateral load resisting systems are widely used in high seismic regions due to their favorable characteristics of high amounts of ductility, relatively low mass, and fast construction. Having large ductility in a structural steel system depends on proper detailing of the connection points and locations of high inelastic strain. As shown by the 1994 Northridge earthquake, improper detailing can lead to stress concentrations and significantly reduce system ductility because of fracture. Additionally, locations of concentrated material inelasticity are susceptible to ultra-low cycle fatigue fracture. An underpinning concept in seismic design is that the structural system deformation capacity is greater than deformation demand. In order to computationally predict the deformation capacity of components, a model must be used that can predict material deterioration and failure. Most common structural analysis techniques are not refined enough to be able to predict member level damage accumulation or loss of load carrying capacity due to fracture. They essentially assume that materials have infinite strain capacity or set a limit on the maximum strain a material can achieve. In order for a computational analysis program to predict damage and fracture under a complex, cyclic loading history, a damage mechanics rule needs to be integrated into the material model.

Damage in ductile metals is due to the formation and coalescence of microvoids, which initiate as a result of fractures or debonding of inclusions from the ductile matrix [1]. Increasing plastic strain causes the microvoids to coalesce and grow in size until the material can no longer carry additional load, which results in fracture. Early micromechanical investigations into the damage evolution of ductile metals were conducted by McClintock [2] and Rice and Tracey [3]. Building on the micromechanical investigations, models have been developed to predict cyclic fatigue fracture. Most of these models can be divided into two major groups. The first group are void volume fraction models; which predict failure when the void volume fraction reaches a critical value. An example of a void volume fracture model is the Rice and Tracey [3] model. The second group, are continuum damage mechanics models and they predict failure when the accumulated damage exceeds a critical value. An example of a continuum damage mechanics model is the Lemaitre ductile damage model [4]. Both types of models can be written in the formwork of stress-modified critical plastic strain as presented in Eq. 1 and Eq. 2 [1].

$$\text{Damage evolution} \quad D = \int F(\sigma) G\left(\dot{\varepsilon}^{p}\right) dt \tag{1}$$

$$\text{Failure criteria} \quad D = D_c \tag{2}$$

Where F is the stress modification function, σ is the stress tensor, G is the plastic strain rate function, $\dot{\varepsilon}^{p}$ is the plastic strain rate tensor, D is the damage of the material, and D_c is the critical damage parameter that delineates failure [1]. The different damage models vary in how they define the stress modification function, F, and the plastic strain rate tensor, G. However, these early models were mostly developed and validated for prediction of monotonic fracture under relatively high stress triaxiality [5]. Recently, these early models have been developed and applied to better capture cyclic loading and low triaxiality stress states.

One such model is the cyclic damage-plasticity model (CDPM) formulated by Huang and Mahin [1]. The specific constitutive law combines the Lemaitre continuum damage mechanics model with the Armstrong-Frederick combined hardening material model to capture the hysteretic response of structural steel. The CDPM is available in the commercial finite element program LS-DYNA [6]. The evolution of the damage variable is governed by the rate equation shown by Eq. 3.

$$\dot{D} = \left\{ \begin{matrix} \left[\dfrac{Y}{S}\right]^{T} \dot{\varepsilon}^{p} \\ 0 \end{matrix} \right\} \text{if} \left\{ \begin{matrix} \dfrac{\sigma_m}{\sigma_{eq}} > -\dfrac{1}{3} \\ otherwise \end{matrix} \right\} \tag{3}$$

$$Y = \frac{1}{2}\varepsilon^{el} : D^{el} : \varepsilon^{el} \tag{4}$$

In Eq. 3, $\dot{D}$ is the rate of the damage parameter, Y is the internal energy density release rate (Eq. 4), D^{el} is the fourth-order elasticity tensor, S is a material constant in energy density units, and t is a dimensionless material constant [1, 4]. The ratio of mean volumetric stress, σ_m, to the effective (Von Mises) stress, σ_{eq}, is the stress triaxiality, T. Eq. 3 implies that damage only accumulates when the volumetric stress is tensile or when it is compressive with a relatively low value, i.e. an absolute value less than 33% of the effective stress.

The Armstrong-Frederick combined isotropic/kinematic hardening rule defines the evolution of the yield stress as a function of equivalent plastic strain. The isotropic portion, shown in Eq. 5, controls the size of the yield surface [7]. In LS-DYNA, the isotropic hardening of the yield surface is set by the hardening parameters H, isotropic modulus, and β, isotropic nonlinearity parameter.

$$\sigma_y = \sigma_{y0} + \frac{H}{\beta}\left[1 - \exp(-\beta\bar{\varepsilon}^{pl})\right] \tag{5}$$

The nonlinear kinematic hardening portion, specifically the evolution of the back-stress tensor, is governed by the rate equation shown by Eq. 6. Where C_j and γ_j are material parameters and n is the plastic flow direction. The law can be degenerated into linear kinematic hardening by setting only one back stress tensor, α, and taking the isotropic parameter, H, and the nonlinear kinematic parameter, γ, as zero.

$$\dot{\alpha}_j = \left(C_j n - \gamma_j \alpha_j\right)\dot{\bar{\varepsilon}}^{p} \tag{6}$$

Once the accumulated damage, D, in the material exceeds a critical damage threshold, D_c, the material fails and the element is removed from the analysis. The CDPM was validated with the results of experimental tests by Huang and Mahin [1] on a full-scale, concentrically braced frame specimen. The finite element model of the specimen was constructed using shell elements. Mesh size was refined to ensure both plastic strain and the damage variable were convergent. The finite element model of the braced frame subassembly accurately predicted crack initiation, crack propagation, and fracture of the beam-to-column connection [1].

This paper explores the capability of finite element analysis based on the CDPM to capture the response and failure of a novel steel shear wall system. It is believed that since a buckling brace in a concentrically braced frame and a panel in shear have similar stress triaxialities (approximately $0 < T < 0.4$) [5], that the CDPM could provide good prediction of damage accumulation and fracture initiation.

2. RS-SPSW Experiments

The present study focuses on a novel structural system; the Ring Shaped – Steel Plate Shear Wall (RS-SPSW). The concept utilizes an advantageous peculiarity of a ring. Specifically, when a ring is deformed into an ellipse, the amount of elongation in one direction is approximately equal to the amount of expansion in the perpendicular direction. Fig. 1a and Fig. 1c show the ring concept applied as a full wall panel and a solid plate subjected to shear displacement, respectively. The ring concept is shown in Fig. 1b, where the longitudinal elongation is δ_1 and the perpendicular contraction is δ_2. Similarly, for a solid plate, the shortening along the perpendicular direction is related to the longitudinal elongation by Poisson's ratio; shown in Fig. 1d. For the RS-SPSW panel, the equal elongation and contraction property of the rings means there is no build-up of resistance along the compression diagonal; which would reduce buckling. For the solid panel, the shortening of the compression diagonal is approximately 0.3-0.5 (Poisson's ratio for steel) of the longitudinal elongation. This would result in a build-up of excess material along the compression diagonal. The build-up of material would cause a compressive force in the perpendicular direction of the tension field; leading to shear buckling of the web plate.

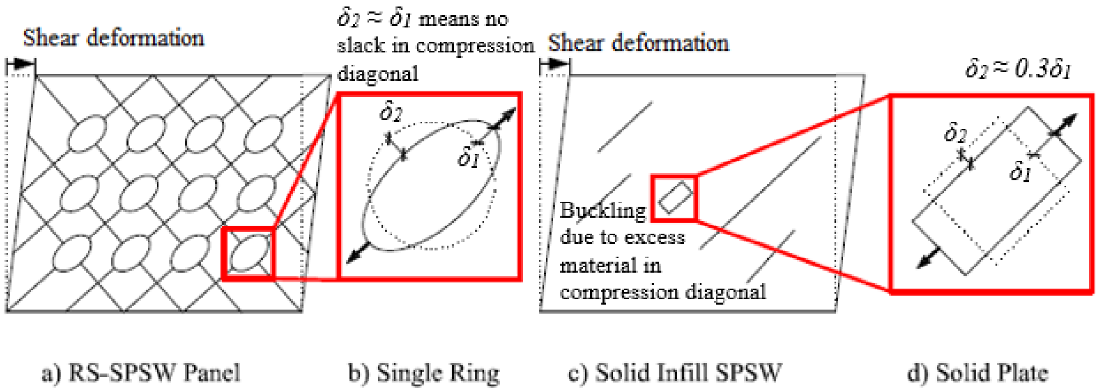

Fig. 1 – Ring Shaped – Steel Plate Shear Wall Concept

Four large-scale experiments were conducted to validate and study the RS-SPSW concept. The tests were two-thirds scale and based off a six-story prototype building located in a high seismic region. The test frame, shown in Fig. 2, was approximately 3 meters (10 feet) wide from column centerline to column centerline by 2.6 meters (8.5 feet) tall from beam centerline to beam centerline. The test frame had pinned beam-to-column and column base connections. The RS-SPSW panels were connected to the boundary frame using double angle, L5x5x5/8, bolted connections with A490 bolts. Specimens had either two, double-angle stiffeners or one, double-angle stiffener evenly placed on the panel to help further restrain global shear buckling. The double-angle, L5x5x5/8, stiffeners were bolted to the infill panel using 3-4 snug tight bolts. A 25 mm gap was left between the end of the stiffener and the boundary elements to allow for movement of the boundary frame. This configuration of stiffeners restrains out-of-plane displacement of the web panel without exerting any additional loads to the boundary members. The experiments were subjected to the ATC-24 pseudo-static, cyclic loading protocol [8].

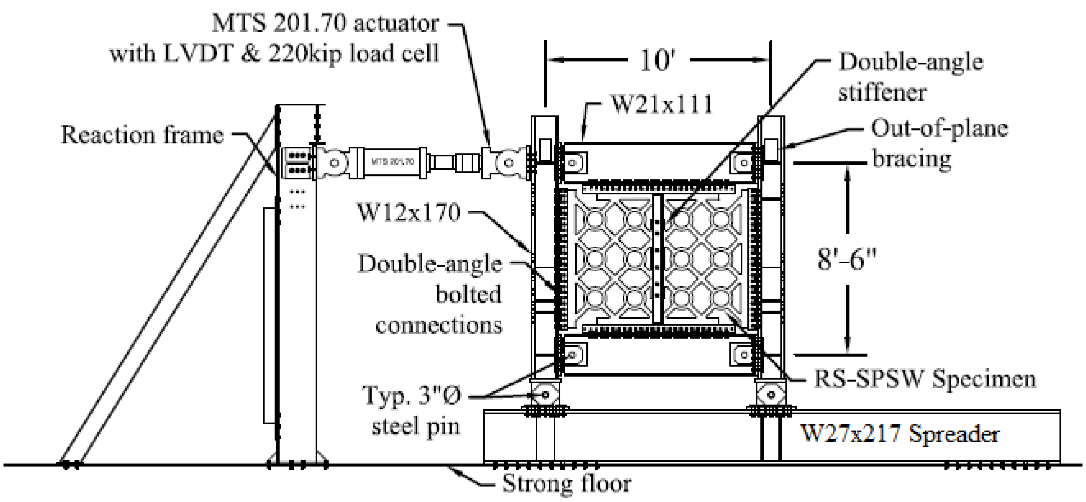

Fig. 2 – RS-SPSW test frame

During the experiment, load was recorded through a load cell in the MTS 201.70 actuator and displacements were recorded through a LVDT in the actuator and 7 wire-potentiometers positioned on the test frame. The test results showed that the panels eventually lost load carrying capacity due to ULCF fractures in multiple rings. To better quantify the fracture mechanism and damage accumulation in the RS-SPSW test specimens, the CDPM was applied to two of the four RS-SPSW specimens which were waterjet cut from the same heat of 3/8” thick A36 material. Since the specimens were fabricated from the same heat of material they should have similar material characteristics. The two RS-SPSW specimens had different geometry, as shown in Fig. 3. Fig. 4 shows the experimental hysteretic behavior of the two RS-SPSW specimens. Note that both specimens formed multiple fractures before losing significant load carrying capacity.

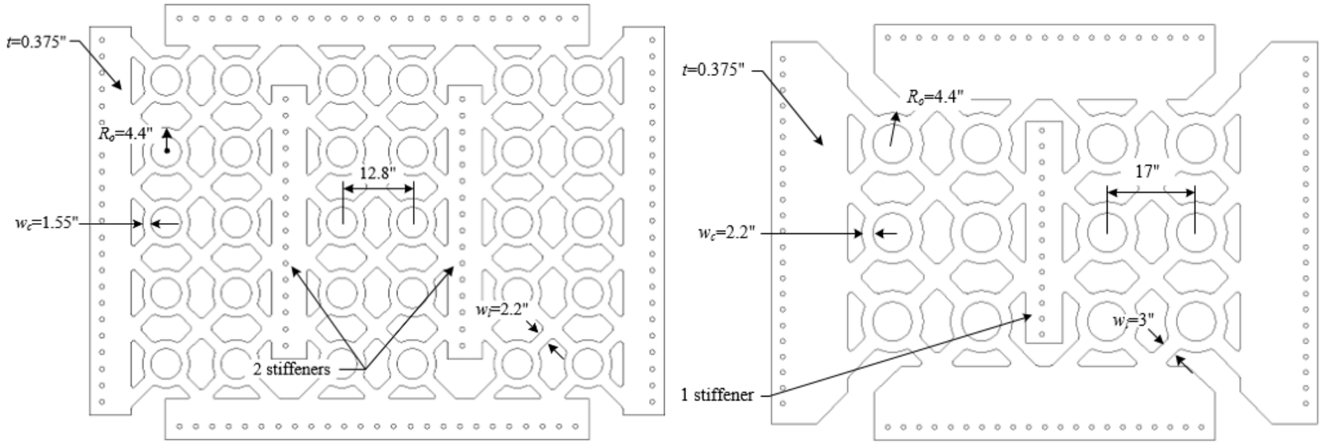

a) Specimen 2 b) Specimen 3

Fig. 3 – RS-SPSW specimens used for fracture study

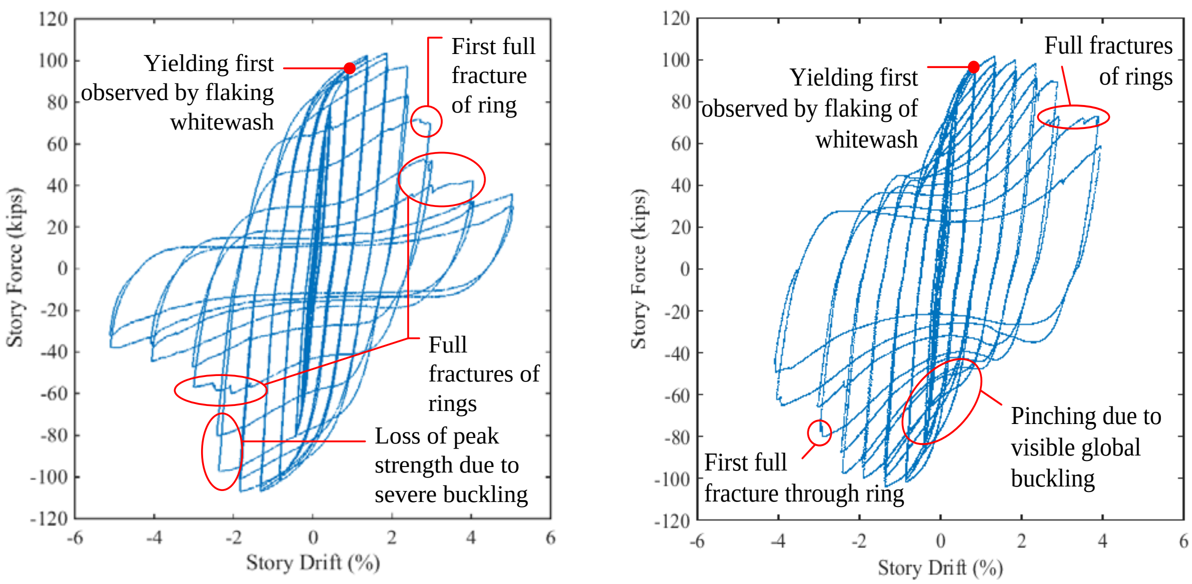

a) Specimen 2 b) Specimen 3

Fig. 4 – Hysteretic behavior of two RS-SPSW specimens

3. CDPM Calibration

The CDPM requires calibration of the nonlinear combined isotropic/kinematic hardening rule and the damage law parameters. The calibration presented used monotonic and cyclic test data from coupons fabricated out of excess over plate material from specimens 2 and 3. The monotonic coupon was a round, reduced-section standard tension coupon that was proportioned based on ASTM E8 guidelines [9]. The cyclic coupons were circumferentially notched tension (CNT) coupons that were based on material tests done by Kanvinde [10] and Myers [11]. Fig. 5a shows the geometry parameters for the CNT coupons. Table 1 displays the measured coupon geometries, the applied strain control displacement protocols, and the number of cycles until failure.

Finite element models of the coupons were constructed utilizing LS-DYNA [6]. The coupons were modeled using axisymmetric quadrilateral elements with the centerline of the cylindrical coupon set as the axis of symmetry, shown in Fig. 5b. A 25.4 mm gage length section of the coupon was modeled since strain over a

25.4 mm gage length extensometer was recorded during the experiments. The gage length section was fixed against x-axis (horizontal) displacement at the right end and the displacement protocol was applied along the x-axis at the left end. These boundary conditions simulate the strain-controlled coupon tests. The CDPM was then calibrated so that the models matched the experimental coupon results and the number of cycles to fracture as closely as possible.

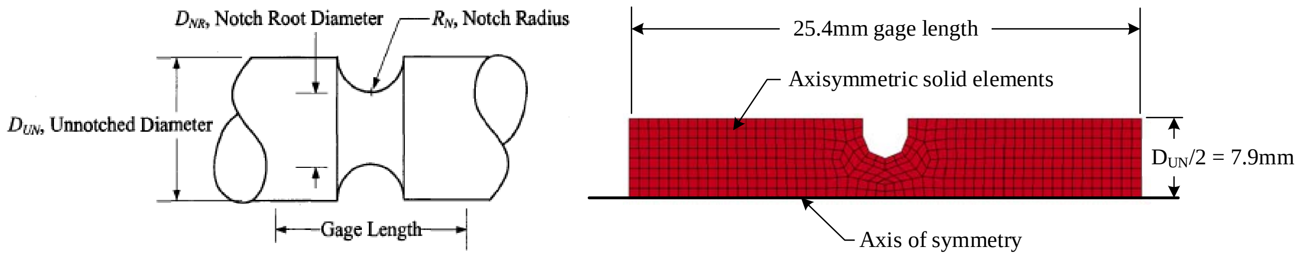

a) Geometry parameters [11] b) axisymmetric finite element model

Fig. 5 – Circumferentially Notched Tension (CNT) coupons

Table 1 – CNT specimen geometry, displacement protocol measured over 25.4mm gage length, and cycles until fracture

Test	D_{UN} (mm)	D_{NR} (mm)	R_N (mm)	Displacement (mm,mm)	No. Cycles to Fracture
Tension	7.92	4.04	n/a	monotonic	n/a
LN1	7.94	3.98	1.86	(0,0.71)	3
LN2	7.91	3.96	1.87	(0,0.51)	7
SN1	7.92	3.90	1.15	(0,0.41)	6
SN2	7.93	4.02	1.11	(0,0.25)	16
SN3	7.90	3.84	1.12	(0.20,0.41)	22

The calibrated values of the elastoplastic and damage model parameters are presented in Table 2, where the variables are the same as in Eq. 3, Eq. 5, and Eq. 6. EPSD is the plastic strain threshold where damage accumulation begins. For the simulations presented, damage accumulation was started at first yield. D_c is the critical damage value where the material fails. The critical damage parameter, D_c, was set to 1.0 as recommended by Dufailly [4]. Fig. 6 shows the monotonic tension coupon true stress versus true strain behavior compared to the calibrated Armstrong-Frederick material model. Fig. 7 and Fig. 8 show the cyclic CNT coupon force versus displacement behavior compared to the axisymmetric CDPM models.

As shown by, Fig. 6, Fig. 7, and Fig. 8 the Armstrong-Frederick material model can satisfactorily capture the cyclic behavior and peak strength of the CNT coupons. The damage model was more challenging to calibrate and more sensitive to the calibration parameters. Only two parameters, S and T, are needed to calibrate the damage model. They were calibrated through a trial and error procedure seeking to minimize the error of number of cycles until fracture across all five CNT coupons. Table 3 shows the number of cycles until fracture of the experimental CNT coupons and the axisymmetric models. Table 3 also shows the percent error between the experimental tests and the computational simulations, where negative error represents over-predicting cyclic fatigue life. Using the damage parameters given in Table 2, the model predicts ULCF of the CNT coupons for low number of cycles until fracture within 1 cycle. However, the error of the CDPM grew as the number of cycles until fracture increased. Additionally, the coupon models did not capture the gradual strength degradation of specimens SN2 and SN3. The model instead fractured quickly as elements were deleted from the simulation.

Table 2 – CDPM calibration parameters

Yield Stress, σ_{yo} (MPa)	E (GPa)	*H* (MPa)	β	C_j (MPa)	γ	EPSD	S	T	D_c
296.5	200	482.6	4	4550.5	20	0	0.75	0.60	1.0

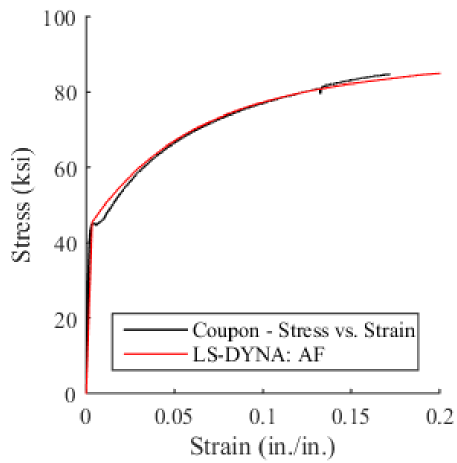

Fig. 6 – Monotonic coupon behavior compared to Armstrong-Frederick (AF) material model

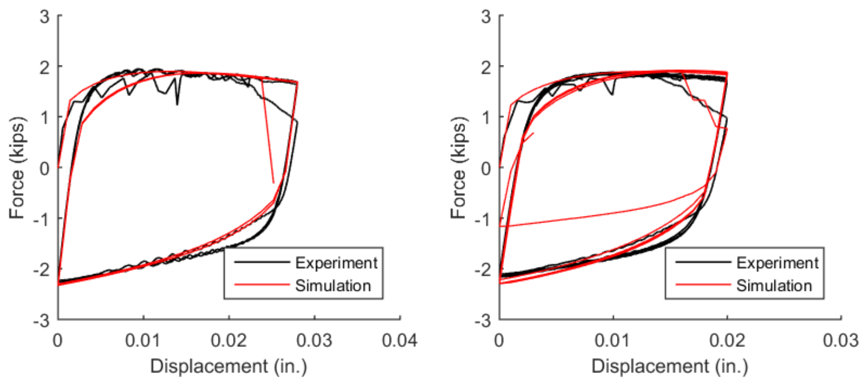

a) LN1 b) LN2

Fig. 7 – Large-Notch CNT coupons compared to CDPM prediction

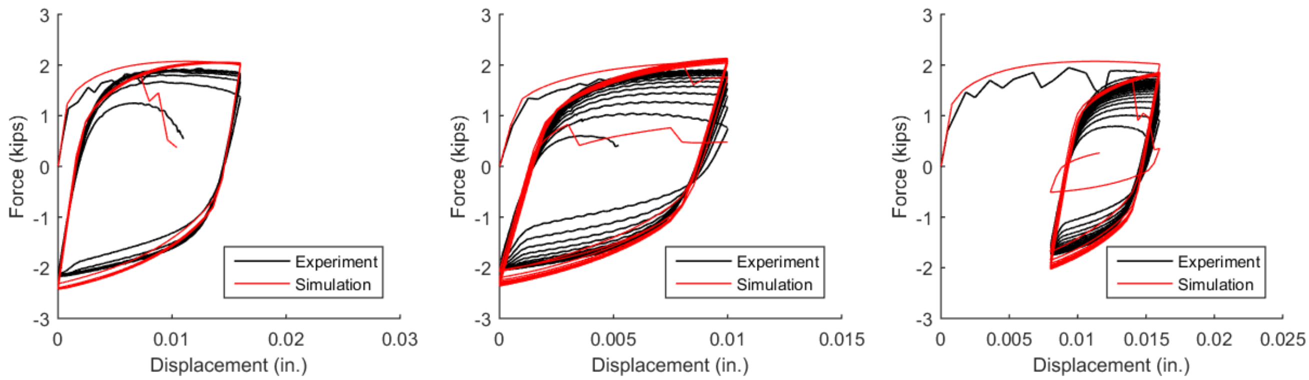

a) SN1 b) SN2 c) SN3

Fig. 8 – Small-Notch CNT coupons compared to CDPM prediction

Table 3 – CNT coupon number of cycles until fracture

Test	Exp. Cycles to Fracture	Model Cycles to Fracture	Error (%)
LN1	3	3.5	-16
LN2	7	6.0	14
SN1	6	6.0	0
SN2	16	13	19
SN3	22	15.5	29

4. RS-SPSW Models

The large-scale RS-SPSW experiments were modeled utilizing LS-DYNA [6]. The RS-SPSW specimen mesh discretization corresponded to a total of four or five elements across the ring width. As shown in Fig. 9, the infill plate was modeled using four-node shell elements based on the formulation of Belytschko and Tsay [12] with five thickness integration points. The boundary members were modeled with beam elements using the formulation of Belytschko and Schwer [13]. A perfect (rigid) connection between the plates and the bounding beams was used. The beam-to-column pin connections were simulated by releasing the rotational degree of freedom at the nodes corresponding to the pin locations. The stiffeners were simulated by fixing the out-of-plane (z-axis) displacement of the nodes on the plate under where the double-angle stiffeners were located. The base pins were represented by fixing all the translational degrees of freedom and the x-axis and y-axis rotation. Lastly, the tops of the columns were restrained against out-of-plane (z-axis) displacement and x-axis and y-axis rotation.

An explicit time stepping routine was utilized to avoid convergence issues once elements started being removed due to the CDPM. For an explicit time integration routine, the prescribed motion is given in relation to time. The critical time step for stability is described by the Courant-Friedricks-Levy criterion, and is the smallest element size divided by the wave propagation velocity. The wave propagation velocity is the square root of modulus of Elasticity divided by material density [14]. Total computational run time can be roughly calculated by dividing the total time of the prescribed motion by the critical time step.

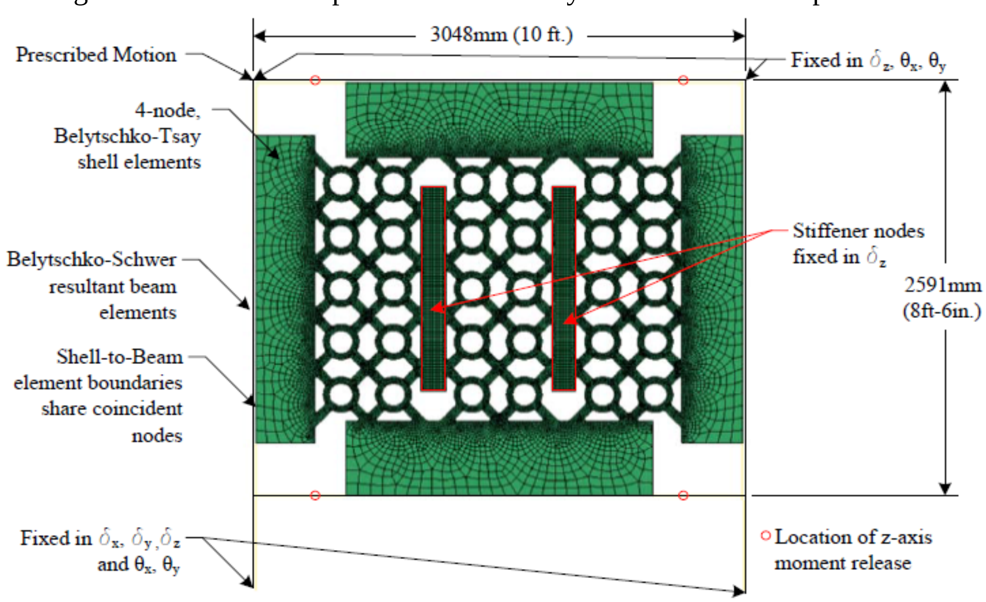

Fig. 9 – LS-DYNA Model of specimen 2

The models were subjected to the experimental cyclic displacement protocol recorded during the tests. Table 4 shows the displacement amplitudes, story drift, number of cycles at each amplitude, the time elapsed by the end of each displacement amplitude during the experiment and during the computational simulation, and the computational model loading rate. The experiments were conducted pseudo-statically, at a loading rate of 25.4 mm/min. (1 in./min) or 0.42 mm/sec. Due to the fine mesh of the RS-SPSW models, the critical time step was approximately 1×10^{-5} seconds. In order to reduce computational run time, the timeframe of the experimental displacement protocol was shortened. Shortening the time over which the displacement protocol was applied shortened the computational run time to approximately 30 hours using 8 SMP (symmetric multi-processing) threads. In order for the models to represent a pseudo-static loading condition, it was ensured that the kinetic energy did not exceed 1 percent of the total system energy.

Table 4 – Displacement amplitudes, story drift, and time elapsed during cycles

Displacement Amplitude (mm)	**Story Drift (%)**	**Number of Cycles**	**Accumulated Displacement at End of Cycles (mm)**	**Experimental Time at End of Cycles (sec.)**	**Simulated Time at End of Cycles (sec.)**	**Simulation Load Rate (mm/sec.)**
+/- 6.35	0.20	3	76.2	180	6.0	12.7
+/- 8.89	0.28	3	182.9	432	14.4	12.7
+/- 13.97	0.44	3	350.5	827	27.5	12.7
+/- 28.45	0.90	3	690.9	1633	47.7	17.0
+/- 43.43	1.37	3	1211.6	2864	78.5	17.0
+/- 59.18	1.87	2	1686.6	3983	97.1	25.4
+/- 75.44	2.39	2	2288.5	5408	120.9	25.4
+/- 93.47	2.96	2	3037.8	7177	150.4	25.4
+/- 125.98	3.98	2	4046.2	9558	190.0	25.4

5. Results

The hysteretic results of the computational analyses compared to the RS-SPSW experiments are shown in Fig. 10. As shown by Fig. 10, the models over-predict peak base shear strength, have early onset buckling, and over-predict the amount of pinching due to buckling. The over-prediction of base shear strength could be due to having too much strain hardening during the analysis.

Previous analyses conducted by the authors utilized a linear kinematic material model, with a gradual strain hardening slope of 1400 MPa, which provided a closer match to the experimental hysteretic response. The computational analyses were conducted using implicit time integration in ABAQUS 6.13 [15]. The finite element models had identical mesh, element formulations, and boundary conditions as the LS-DYNA explicit models described above. The ABAQUS models predicted peak shear strength at 1 percent story drift within 7 percent.

Furthermore, the CDPM simulation of Specimen 2, shown in Fig. 10a, did not show any fractures by the end of the displacement protocol. The model of Specimen 3 predicted fracture initiation at the second positive peak of 4 percent story drift. By the end of the analysis, no other fractures had initiated and the existing fracture had only propagated half-way through the ring. Fracture initiation was determined as the story drift where the first element was removed from the analysis. Both experimental specimens had multiple full fractures through the rings by the beginning of the 4 percent story drift cycles.

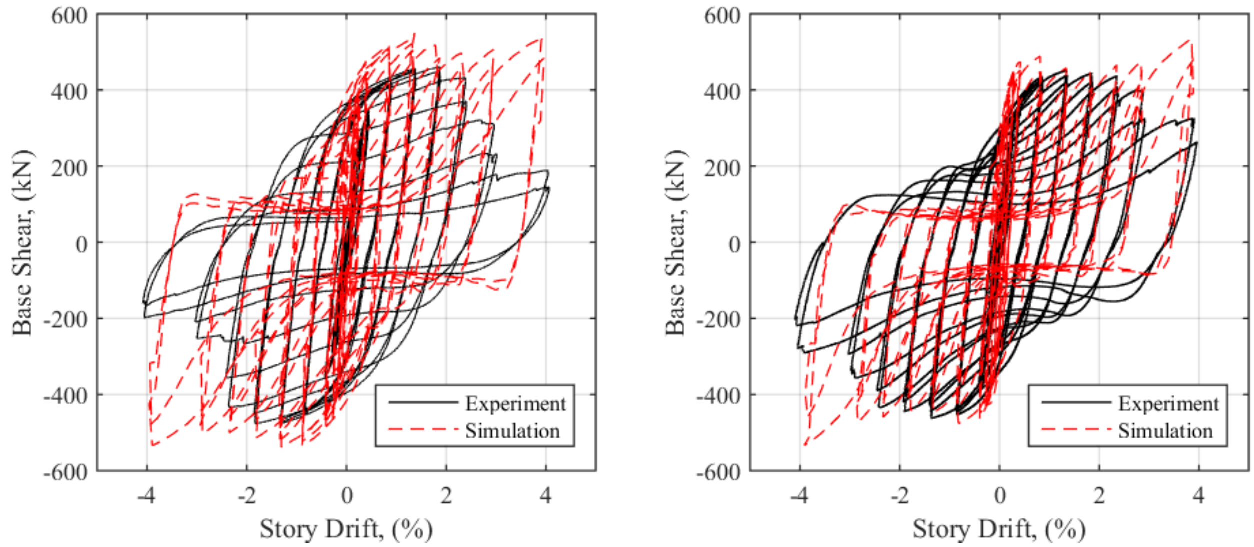

a) Specimen 2 b) Specimen 3

Fig. 10 – Hysteretic comparison between experimental results and LS-DYNA simulation

One possibility for the CDPM not closely predicting fracture of the experiments is that the buckling of the infill panel during the computational simulation could have caused the plastic strain to accumulate differently than in the experiment. This could lead to lower damage accumulation. Additionally, the damage model was calibrated using CNT coupons which have much higher triaxiality than a thin web plate loaded in shear. This could also lead to lower damage accumulation. The influence of triaxiality on damage accumulation is well documented [3, 4], so it is possible that the CDPM damage model was not adequately calibrated through the use of CNT coupons.

In an attempt to get a better prediction of the experimental results, the CDPM calibration parameters were modified based on the recommended default values from Huang and Mahin [1]. The elastoplastic material model was modified to match the linear kinematic material model used in the ABAQUS simulations. Using the Huang and Mahin report, the damage parameter T was set equal to 1.0 and S was set to $\sigma_{y0}/200$ (with yield stress in ksi) or 0.215. The time over which the loading protocol was applied was also increased to 2402 seconds, and the computational run time was given an upper bound of 144 hours using 16 SMP threads.

Fig. 11 shows the modified CDPM models compared to the experimental results. The specimen 2 model completed up to the first positive 2.5 percent story drift cycle by the end of the 144 hour run time. This is due to the small critical time step ($9.26\text{x}10^{-6}$ seconds) and large number of shell elements (~70,000). However, despite not completing the full displacement protocol, it is apparent from comparing Fig. 10a and Fig. 11a that linear kinematic hardening better matches the peak base shear force than Armstrong-Frederick. Additionally, with the modified damage parameters, fracture initiation occurred after the 3rd positive 1.5 percent story drift cycle; which is approximately 2 cycles before fracture initiation was noticed during the experiment. By the end of the simulation, fractures had initiated in every ring in the top and bottom rows; which was the fracture pattern observed during testing.

Linear kinematic hardening under predicted the peak shear strength for specimen 3. It was also observed that the peak shear force is smaller in the explicit analysis than in the previously conducted implicit analyses; even though the same elastoplastic constitutive model was used. Both CDPM models still predict the onset of buckling earlier than observed during the experiment and show greater pinching of the hysteresis. The CDPM model predicted fracture initiation in specimen 3 during the 1st positive 2 percent story drift cycle; which is 4 cycles earlier than observed during the experiment. By the 1st positive 4 percent story drift cycle the four corner rings had fractures that extended approximately halfway through the ring width. The experimental specimen at the same drift level had formed full fractures through the entire ring width at those locations. By the end of the analysis, only the top right corner ring had fractured through its width. The fracture pattern from the simulation matched the fracture pattern observed during the experiment. Curiously, even though fractures were occurring in the model, the peak base shear strength was not decreasing as observed during the experimental tests.

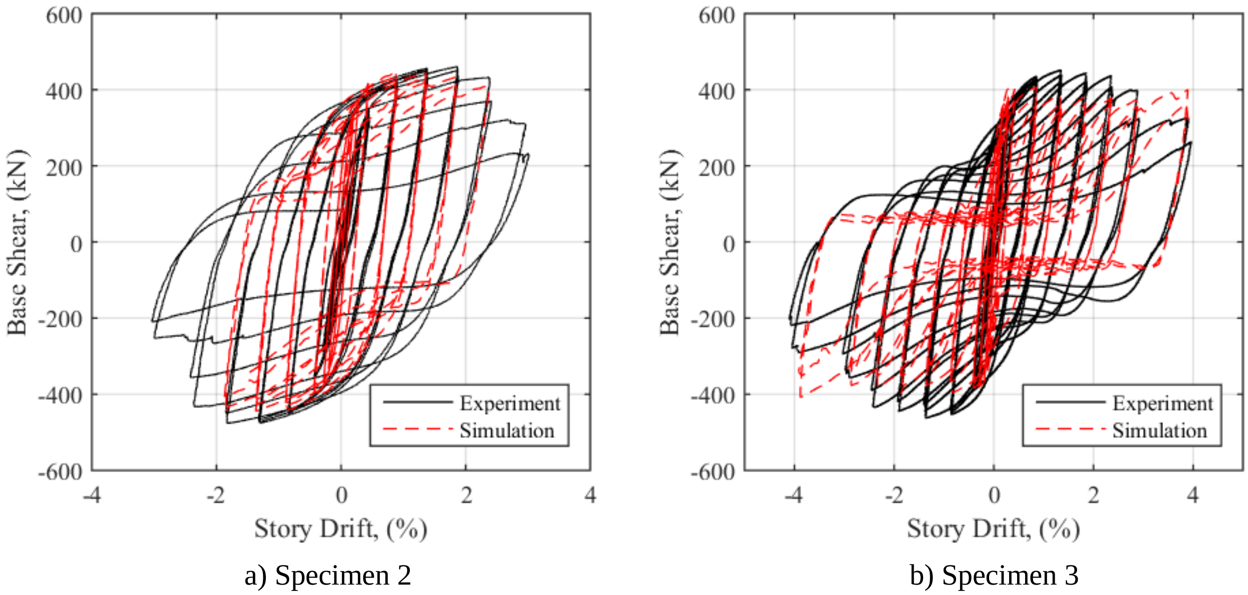

Fig. 11 – Hysteretic comparison between experimental results and CDPM model using linear kinematic hardening and modified damage parameters

6. Discussion and Conclusion

Based on the results from the computational analyses, there is need for improvement in the application of the CDPM. Calibrating the CDPM using cyclically loaded CNT coupons did not result in an accurate prediction of the cycle at fracture initiation or the fracture propagation in the specimens. Using the Huang and Mahin [1] recommended default CDPM values of *S* equals 0.215 and *T* equals 1.0 provided a better prediction of fracture initiation, but still under predicted the rate of fracture propagation. Given the challenges described above it is recommended that the following be studied more closely in relation to implementing the CDPM:

(1) Development of an effective calibration method for the Armstrong-Frederick hardening material model. In this study, it was shown that the Armstrong-Frederick model closely predicted the uniaxial, cyclic behavior of tension coupons and yet over predicted peak shear force of the large-scale RS-SPSW infill panels at 1 percent story drift by approximately 20% for specimen 2 and 10% for specimen 3.

(2) The effect of calibrating the damage model parameters using tests on coupons with much higher triaxiality than that of the structural members being studied. Using the calibrated damage parameters resulted in analyses that didn't initiate fracture until the end of the loading protocol. Modifying the fracture parameters so that damage would accumulate much quicker improved the fracture initiation prediction but still under estimated the fracture propagation rate.

(3) Using a linear kinematic hardening rule with a hardening slope of 1400 MPa and an implicit time integration routine over predicted the peak shear strength by approximately 7 percent at 1 percent story drift. Switching to an explicit time integration routine caused the specimen 3 model to under predict the peak strength by approximately 12%. Additionally, the explicit analyses displayed much greater pinching of the hysteresis due to buckling than the implicit analyses. The influence of explicit time integration on buckling of thin-walled members has

been explored in the literature [16]; but it is recommend that additional work focusing on buckling of slender plates loaded in shear be conducted.

Overall the CDPM has the potential to be a powerful analysis tool when analyzing structural elements for ultra-low cycle fatigue fracture. Overcoming the challenges described above would make large step in developing robust ULCF fracture models that can be used to analyze complex, nonlinear systems.

7. Acknowledgements

This material is based upon the work supported by the National Science Foundation under Grant No. (CMMI-1453960). Any opinions, findings, and conclusions or recommendations expressed in this material are those of the authors and do not necessarily reflect the views of the National Science Foundation or other sponsors. Additionally, this research was supported by AISC through the Milek Faculty Fellowship Program, and in-kind donations from Banker Steel Inc., Weinstock Brothers of New York, and Applied Bolting Inc.

8. References

[1] Huang, Y. and Mahin, SA (2010): Simulating the inelastic seismic behavior of steel braced frames including the effects of low-cycle fatigue. *PEER Report 2010/104,* University of California, Berkeley, Berkeley, CA.

[2] McClintock, F.A. (1968). A criterion for ductile fracture by the growth of holes. *Journal of Applied Mechanics,* 35, 363-371.

[3] Rice, J.R. and Tracey, D.M. (1969). On the ductile enlargement of voids in triaxial stress fields. *Journal of Mechanics and Physics of Solids,* 17, 201-217.

[4] Dufailly, J. and Lemaitre, J. (1995). Modeling very low cycle fatigue. *International Journal of Damage Mechanics,* 4, 153-170.

[5] Smith, C.M., Deierlein, G., and Kanvinde, A.M. (2014). A stress-weighted damage model for ductile fracture initiation in structural steel under cyclic loading and generalized stress states. *Blume Earthquake Engineering Center Report No. 187,* Stanford University, Stanford, CA.

[6] LSTC (2007). *LS-DYNA Keyword User's Manual,* Livermore Software Technology Corporation, CA, US.

[7] Armstrong, P.J. and Frederick, C.O. (1966). A mathematical representation of the multiaxial bauschinger effect. *CEGB Report RD/B/NN/731*, Berkeley Laboratories, R&D Department, Berkeley, CA.

[8] ATC. (1992). Guidelines for cyclic seismic testing of components of steel structures for buildings. *Report No. ATC-24*, Applied Technology Council, Redwood City, CA.

[9] ASTM (1924). Standard test methods for tension testing of metallic materials. *E8/E8M – 15a,* ASTM, Philadelphia, PA.

[10] Kanvinde, A. (2004): Micromechanical simulation of earthquake-induced fracture in steel structures. *PhD Dissertation*, Stanford University, Stanford, CA.

[11] Myers, A. (2009): Testing and probabilistic simulation of ductile fracture initiation in structural steel components and weldments. *PhD Dissertation,* Stanford University, Stanford, CA.

[12] Belytschko, T.B. and Tsay, C.S. (1984). Explicit algorithms for nonlinear dynamics of shells. *Computer Methods in Applied Mechanics and Engineering*, 43, 251-276.

[13] Belytschko, T.B., Schwer, L., and Klein, M.J. (1977). Large displacement transient analysis of space frames. *International Journal for Numerical Methods in Engineering,* 11(1), 65-84.

[14] Belytschko, T., Liu, W.K., Moran, B., and Elkhodary, K.I. (2014). *Nonlinear Finite Elements for Continua and Structures,* John Wiley & Sons.

[15] Dassault. (2013). *Abaqus version 6.13 Documentation,* Dassault Systems, 11, Rue Marcel Dassault, 78140 Velizy Villacoublay, France

[16] Rust, W. and Schweizerhof, K. (2003). Finite element limit load analysis of thin-walled structures by ANSYS (implicit), LS-DYNA (explicit), and in combination. *Thin-Walled Structures*, 41, 227-244.